Full Length Article

Modulation of Molybdenum oxidation state via Catalytic-oxidation

Kangchun Lee [a], Seho Sun [b], Hyunseok Ko [c], Sung Beom Cho [d], Ganggyu Lee [b], Dongsoo Lee [b], Taeseup Song [b,*], Ungyu Paik [b,*]

[a] Foundry Process Development Team, Semiconductor R&D Center, Samsung Electronics, Hwaseong, South Korea
[b] Department of Energy Engineering, Hanyang University, Seoul, South Korea
[c] Center of Materials Digitalization, Division of Carbon Neutrality & Materials Digitalization, Korea Institute of Ceramic Engineering and Technology (KICET), Jinju, South Korea
[d] Department of Materials Science and Engineering, Ajou University, Suwon, South Korea
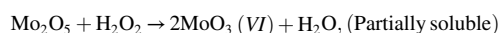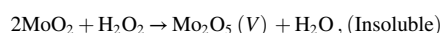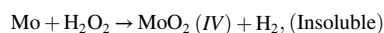
ARTICLE INFO

ABSTRACT

Molybdenum (Mo) is a promising metal contact material to replace tungsten due to its low electrical resistivity in sub-3 nm next-generation semiconductor processes. However, the high dissolution rate of Mo during the chemical mechanical planarization (CMP) process limits its practical introduction because it deteriorates surface flatness and consequently causes decisive device failure. Herein, we report a strategy to suppress Mo dissolution by manipulating the oxidation state of Mo film via catalytic-oxidation reaction. Adoption of Fe catalyst under the trace amounts of H_2O_2 enables the formation of insoluble MoO_2 and Mo_2O_5 phases while minimizing the generation of the soluble MoO_3 phase. The dissolution behaviors of Mo at various oxidation states were investigated according to both oxidizer and catalyst concentrations during the CMP process. To identify the detailed dissolution phenomena of Mo, the Gibbs free energies and dissolution kinetics in different Mo oxide phases were validated using density functional theory (DFT) calculation. We successfully confirmed that catalytic-oxidation using Fe ions achieved an enhanced removal rate from 780 to 1500 Å/min, even though the dissolution rate was minimized from 636 to 57 Å/min compared to a single oxidation reaction. We believe that our results, supported by theoretical considerations and experimental results, can elucidate Mo oxidation and dissolution phenomena for application to the advanced semiconductor manufacturing processes.

1. Introduction

The development of nanoscale semiconductor processing has been driven by the structural innovation of devices and application of new materials for the past two decades. In particular, during the era of sub-3 nm gate-all-around field-effect-transistor (GAAFET) devices, as the contact poly pitch (CPP) is shrunk to less than 50 nm, tungsten in the middle of line (MOL) process faces a threshold due to the sharp increase in resistivity. Therefore, the demand for the introduction of new contact materials has constantly required to realize advanced device performance with high speed and low power consumption. From this point of view, Molybdenum (Mo, resistivity: 5.3 μΩ·cm) has received considerable attention as a candidate to replace tungsten (W, resistivity: 5.6 μΩ·cm) due to its low electrical resistivity in next-generation semiconductors for MOL via contact (Fig. 1(a)) [1–4]. The Mo contact scheme in ultra large scale integration (ULSI) is achieved through chemical mechanical planarization (CMP) followed by Mo deposition

via chemical vapor deposition (CVD). As with general metal CMP processes in materials such as copper, tungsten, ruthenium, and cobalt, it is also difficult to directly polish Mo film due to its high mechanical strength. Similarly, in Mo CMP, the metal oxide layer should be formed on the surface by oxidation using hydrogen peroxide (H_2O_2), and CMP is performed by tearing off the weak interface of metal/metal oxide [5–7]. Many previous studies focused on adopting H_2O_2 as an oxidizer in metal CMP applications, including Mo [2,6,8–13]. However, since H_2O_2 is a strong oxidizer at universal pH regions, the formulation of Mo (VI) oxide (i.e. MoO_3) phase with a high oxidation state is inevitable, as illustrated by the following reaction formulas.

$$Mo + H_2O_2 \rightarrow MoO_2\ (IV) + H_2,\ \text{(Insoluble)}$$

$$2MoO_2 + H_2O_2 \rightarrow Mo_2O_5\ (V) + H_2O,\ \text{(Insoluble)}$$

$$Mo_2O_5 + H_2O_2 \rightarrow 2MoO_3\ (VI) + H_2O,\ \text{(Partially soluble)}$$

---

* Corresponding authors.
   E-mail addresses: tssong@hanyang.ac.kr (T. Song), upaik@hanyang.ac.kr (U. Paik).

$$MoO_3 + H_2O \rightarrow H_2MoO_4 \ (VI), \text{(Partially soluble)}$$

$$H_2MoO_4 + 2OH^- \rightarrow 2H_2O + MoO_4^{2-} \ (VI), \text{(Completely soluble)}$$
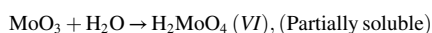
Given that MoO_3 not only has a solubility of 4.9–70 g/L at room temperature but also exhibits chain reactions to the soluble phase of H_2MoO_4 when in contact with H_2O_2, excessive oxidation of Mo is a critical problem that causes defects such as Mo dissolution and pitting corrosion during the CMP process (Fig. 1(b)). Therefore, identifying the redox behavior of Mo is important to ensure the device performance and reliability. Nevertheless, studies on the various phases of Mo oxide, thermodynamically stabilized phase analysis, and dissolution kinetics of Mo oxidation behavior in the semiconductor process are insufficient. Despite Yang et al. [2] once reported the glycine as an inhibitor to prevent Mo dissolution, there are few previous studies to suppress Mo dissolution. Furthermore, the use of additional excess inhibitor has a limitation because it can result in metal–organic residue defects in the overall semiconductor process [14–17] and deteriorate the dispersion stability of CMP slurries [18,19].

In this study, we first clarify a novel strategy for modulating the oxidation state of Mo film via catalytic-oxidation reactions. Only insoluble MoO_2 and Mo_2O_5 phases were obtained, instead of the soluble MoO_3 phase, after the adoption of Fe catalyst in a trace amount of H_2O_2. At the same time, the use of Fe catalyst based on the Fenton reaction [20–23] enhanced the oxidative potential of H_2O_2 by increasing the efficiency of hydroxyl radical generation to support the promotion of MoO_2 and Mo_2O_5 rather than not MoO_3, leading to dissolution-free CMP performances. The formation of various Mo oxide phases and oxidation states of Mo film were analyzed by X-ray photoelectron spectroscopy (XPS). Thermodynamic free energies according to the various oxidation state of Mo oxide formation under the use of Fe catalyst was approximated by energetics from density functional theory (DFT) calculations. The dissolution behavior of each Mo oxide phase was investigated by examining the oxygen vacancy formation energy on top of the Mo surface and confirmed by measuring the corrosion current (I_{corr}) from the potentiodynamic polarization curve.

2. Experimental section

2.1. Material preparation

High purity colloidal silica (d_{mean}: 30 nm, Fuso, Japan) with 3.0 wt% was adopted as a slurry abrasive. In addition, 30 wt% of hydrogen peroxide (H_2O_2, Daejung Chemical, Korea) and Iron(III) nitrate non-ahydrate (Sigma Aldrich, USA) were used as an oxidizer and catalyst, respectively. Malonic acid (M_w: 104.06, Sigma Aldrich, USA) was employed as a slurry stabilizer at 5 mM concentration. Slurry pH was adjusted to 2.0 using nitric acid (HNO_3, 1.0 N, Daejung Chemical, Korea). We obtained molybdenum films on 300 mm wafers (p-Si substrate / thermal oxide 1 kÅ / Ti 0.3 kÅ / Mo 200 nm) manufactured by chemical vapor deposition from Advantec Korea., ltd.

2.2. Surface characterization

The surfaces of Mo films were characterized through XPS (K-Alpha+, Thermo Fisher Scientific Messtechnik, USA) and potentiodynamic polarization measurement (AUT320N, Metrohm AUTOLAB, Switzerland). Experimental samples of Mo film coupon were dipped into 200 mL of various design of experimental conditions at pH 2.0 for 3 min. Subsequently, all of the Mo film samples were rinsed with deionized water and native oxide was removed using buffered oxide etch (BOE) solution before each experiment. The size of cut samples for potentiodynamic polarization measurement was 3×6 cm (exposing an 18 cm^2 active area) and used as a working electrode. The reference and counter electrodes were Ag/AgCl (containing 3 M KCl) and platinum (Pt), respectively. The surface morphologies of Mo films were investigated through atomic force microscopy (AFM) (XE-150, Park Systems, Korea) in a 5×5 μm^2 area with non-contact mode.

2.3. Analysis of hydroxyl radicals

UV–visible measurement (Cary 5000, Varian, USA) was performed to analyze the amount of hydroxyl radicals. 0.04 mM of p-nitro-sodimethylaniline (p-NDA) (Sigma Aldrich, USA) solution was added to each experimental samples to observe the efficiency of hydroxyl radical generation through reaction with H_2O_2. In all the case of the samples, the background measurement was confirmed by the sample without p-NDA.

2.4. Theoretical analysis

The free energy diagram was constructed based on the reaction Gibbs free energy using energetics from DFT calculations [24,25]. Using the values presented in Table 1, the free energies of formation of MoO_2, Mo_2O_5 and MoO_3 phases can be expressed as a Nernst equation as $\Delta_r G = \Delta_r G^0 + RT \ln Q$ where $\Delta_r G^0 = \sum_{products} \Delta E^0 - \sum_{reactants} \Delta E^0$, and Q is
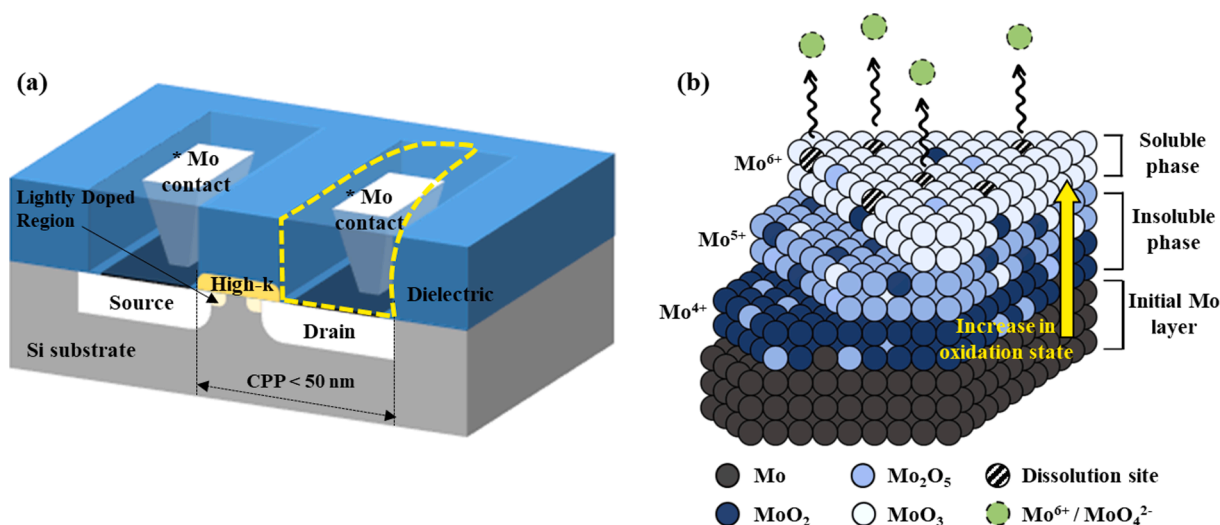

Fig. 1. Schematic illustration of: (a) molybdenum via contact of MOSFET in the MOL process, (b) dissolution behavior of MoO_x during the CMP process.

Table 1
Formation free energies of each chemical species by DFT calculation.

Species	ΔE_F [eV/f.u.]
Mo	0
MoO_2	−6.42
Mo_2O_5	−13.96
MoO_3	−8.07
H_2O	−2.46
H_2O_2	−1.98

the reaction quotient. This can be re-written for aqueous pH solution in terms of activity, $\Delta_r G = \Delta_r G^0 + 2.303 RT \bullet \log\left[\left(a_{H_2O_2}\right)^{-1}\right] -2.303 RT \bullet pH$, where $a_{H_2O_2}$ is the activity of H_2O_2 [26].

For the dissolution of Mo oxides, surface vacancy formation energies are calculated for Mo- and O- using DFT calculations. All DFT calculations were performed using the Vienna Ab-Initio Simulation Package (VASP) [27]. VASP calculations were carried out using the projector-augmented plane-wave (PAW) method [28–31] and the generalized gradient approximation (GGA) exchange–correlation potentials, parameterized by Perdew, Burke, and Ernzerhof (PBE) [32]. The energy cut-off was set as 520 eV, the Brillouin zone was sampled with $3 \times 3 \times 1$ Monkhorst-pack mesh, and dipole corrections [33] were made to correct the effect of the electric dipole on the surface of the finite cell. The formation energy of surface vacancy is calculated as $E_{V_i} = E_d - E_p + \mu_i$, where i is the species of vacancy-site (Mo or O), μ_i is the chemical potential of species i (the range for μ values are chosen for the condition in which all Mo oxides are stable, as shown in Figure S1), and E_d and E_p are energies of defective and pristine slabs, respectively.

2.5. CMP performance evaluation

A coupon CMP polisher (POLI-300, G&P Technology, Korea) with a pad (IC1010 / Suba IV, Rohm, and Haas Electronic Materials, USA) was used for CMP performance evaluation. The thickness of molybdenum films was measured using a four-point probe (FFP) (CMT-SR5000, Changmin Tech, Korea). The specific resistance (ρ) of Mo was assumed to be 5.3×10^{-8} Ω·m and thickness was calculated by dividing by the estimated sheet resistance through FFP in a constant condition. CMP evaluation to obtain material removal rates of Mo films was repeated three times under the following conditions: pressure of 1.5 psi, rotation speed of 79/80 rpm, and flow rate of 100 mL/min.

3. Results and discussion

3.1. Surface analysis and thermodynamics of Mo oxidation states

XPS analysis was performed to clarify the oxidation state and changes in chemical composition of the Mo surface after being immersed for 3 min in different oxidizer and catalyst concentrations. Figs. 2 and 3 show the complete survey of XPS spectra and de-convolution species of Mo 3d elements at pH 2. The high resolution spectra of the Mo 3d peak was de-convoluted into Mo $3d_{5/2}$ and Mo $3d_{3/2}$ using the reference spectra of the single-phases of MoO_2, $Mo_2O_{5,}$ and MoO_3 [34–36]. The peak at 228.2 eV and the smaller peak at 231.5 eV represent metallic Mo. The binding energy peaks for MoO_2 (IV) were detected at 229.2 eV and 232.4 eV. Both 230.8 eV and 234.0 eV peaks signify Mo_2O_5 (V) and the two symmetric peaks at 232.5 eV and 235.6 eV are assigned to MoO_3 (VI) [37]. Figure S2 and S4 represent the de-convoluted high resolution spectra of O 1 s peak. The binding energy peaks at 530.0 eV, 530.5 eV and 530.8 eV correspond to the MoO_3, Mo_2O_5 and MoO_2, respectively [38,39]. O 1 s spectra at 532.7 eV and 533.5 eV are attributed to C═O and C─O bonds [40–42].
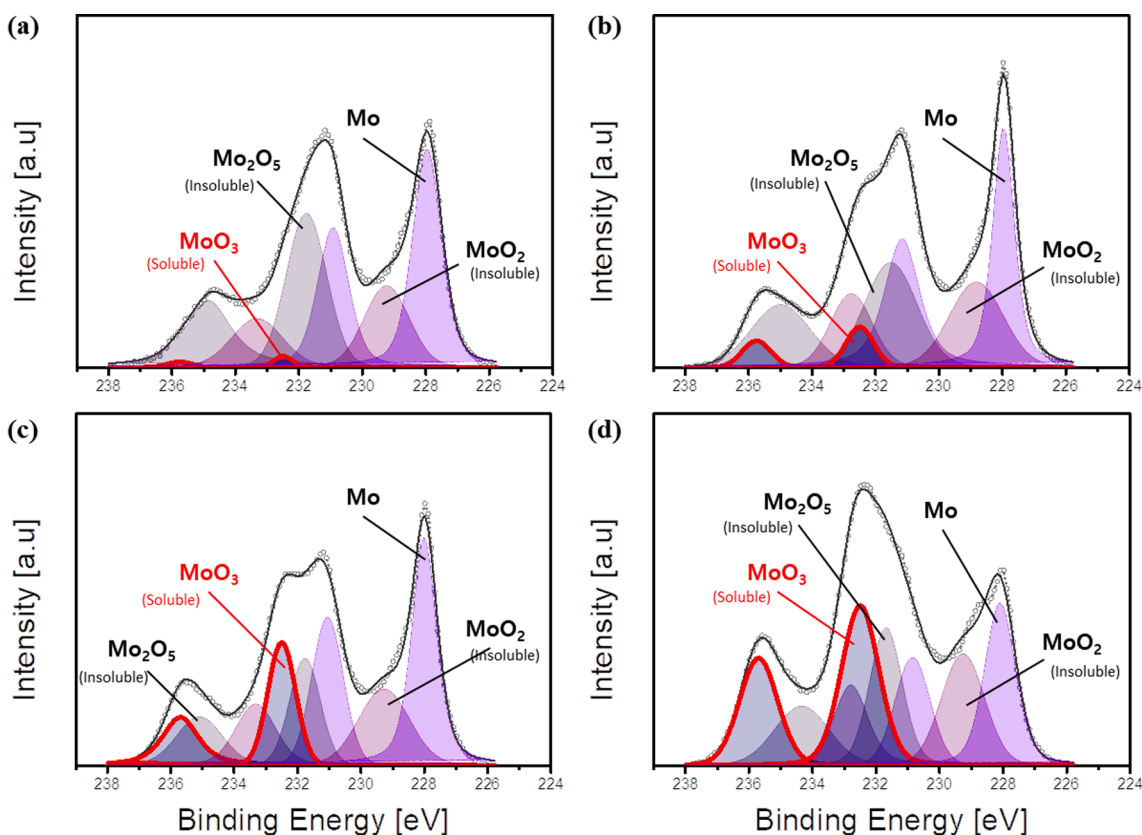
Fig. 2. X-ray photoelectron spectroscopy (XPS) of Mo 3d immersed in different concentrations of H_2O_2: (a) 0.01 M, (b) 0.05 M, (c) 0.1 M, and (d) 0.5 M.
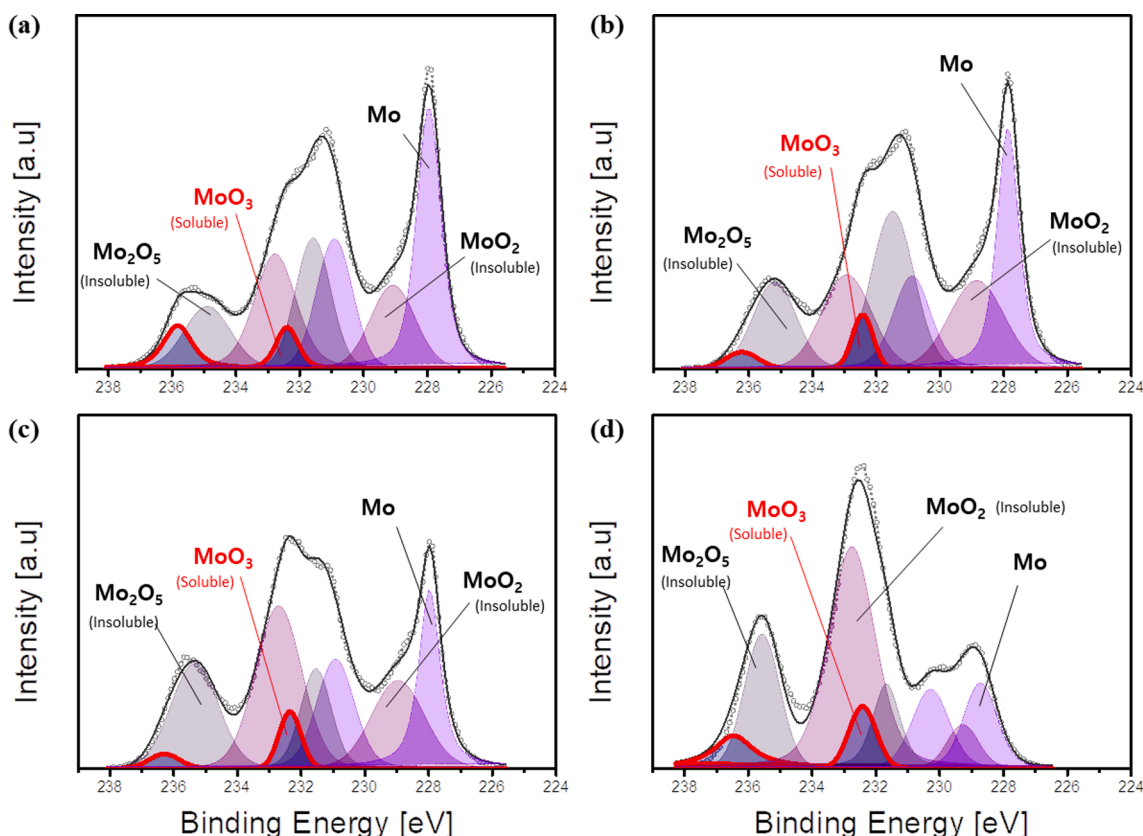
Fig. 3. X-ray photoelectron spectroscopy (XPS) of Mo 3d immersed in different concentrations of Fe(NO3)3: (a) 0.0005 M, (b) 0.0015 M, (c) 0.003 M, and (d) 0.01 M.

Fig. 2 shows the oxidation behaviors of Mo films with 5 mM of Fe catalyst (i.e., Fe(NO$_3$)$_3$) under various conditions of H$_2$O$_2$, a strong oxidizing agent. Without the H$_2$O$_2$ oxidizer, excessively oxidized Mo^{6+} ion from the MoO$_3$ is rarely observed because the oxidation reaction depends on a trace amount of Fe catalyst. However, most of Mo oxides exist only as pristine Mo metal, Mo^{4+} ion (from MoO$_2$) and Mo^{5+} ion (from Mo$_2$O$_5$) (Fig. 2a). However, when the concentration of H$_2$O$_2$ is increased from 0.05 M to 0.5 M, the amount of oxidized Mo film increases and the ratios of Mo oxide forms having large oxidation numbers also increase. Therefore, the ratio of pristine Mo metal state gradually decreases, while the proportion of Mo oxide increases. In addition, the proportion of the soluble Mo^{6+} (MoO$_3$) phase, which was much more oxidized, increased significantly even in the form of equivalent Mo oxide (Fig. 2b-d). Additionally, as shown in Figure S2, the soluble MoO$_3$ phase is continuously detected and maintained regardless of the H$_2$O$_2$ concentration due to the excessive oxidation reaction of Mo, except for infinitesimal of H$_2$O$_2$ 0.01 M.

Fig. 3 presents the oxidation behaviors of Mo films with 50 mM of H$_2$O$_2$ oxidizer under various Fe catalyst conditions. As demonstrated in Figure S3, the Fe catalyst increases the efficiency of hydroxyl radical formation (•OH) by promoting the decomposition of H$_2$O$_2$ [43,44]. Therefore, higher Fe concentration leads to improved H$_2$O$_2$ decomposition efficiency even with the same amount of H$_2$O$_2$ oxidizer (Figure S3). Consequently, the peak area of pristine Mo continuously decreases following the same trend shown in Fig. 2, while the overall peak proportion of the Mo oxide form increases. However, there is a significant difference compared to Fig. 2 in terms of the type of increased Mo oxide that forms. The peak area of the soluble Mo^{6+} (MoO$_3$) phase rarely changes, while the ratio of insoluble Mo^{4+} (MoO$_2$) and Mo^{5+} (Mo$_2$O$_5$) forms increase significantly. In contrast to the circumstances with excessive H$_2$O$_2$, this result suggests that the synergistic effect of the catalytic-oxidation reaction through the addition of Fe catalyst with H$_2$O$_2$ 50 mM enables the formation of the insoluble Mo oxide phase by

modulating the degree of Mo oxidation. Referring to Figure S4, in terms of the types of Mo oxide phases, insoluble MoO$_2$ or Mo$_2$O$_5$ were confirmed under all experimental conditions, while the proportion of soluble MoO$_3$ was attenuated.

3.2. Thermodynamic free energies of Mo oxide phases

Fig. 4(a) illustrates the dependence of pH and H$_2$O$_2$ activity ($a_{H_2O_2}$) on the free energies of Mo oxide phases under the Fe catalyst conditions. With the increase in the concentration of Fe catalyst, the decomposition of H$_2$O$_2$ into hydroxyl radicals is promoted and as a result, $a_{H_2O_2}$ increases. Except for MoO$_2$, in the case of Mo$_2$O$_5$ and MoO$_3$, the free energy of Mo oxide generation is not significantly affected by the pH variable because the sensitivity of pH is thermodynamically insignificant. In particular, with fixed pH 2 value with the Fe catalyst conditions for the CMP process as in Fig. 4(b), the formation of MoO$_2$ and Mo$_2$O$_5$ are endothermic with negative free energies for a broad range of $a_{H_2O_2}$. In other words, under such pH conditions, the formation of MoO$_2$ and Mo$_2$O$_5$ phases are thermodynamically favorable regardless of the concentrations of H$_2$O$_2$ oxidizer. On the contrary, the free energy of the MoO$_3$ formation reaction could be converted to a positive value when $a_{H_2O_2}$ is decreased, indicating that the MoO$_3$ phase is no longer stable and no longer generated. These findings for thermodynamic free energies are consistent with the experimentally observed ratios of Mo oxide phases, as shown in Table 1.

3.3. Kinetics of dissolution behavior according to Mo oxidation state

Potentiodynamic polarization measurements were carried out to investigate the oxidation and dissolution behaviors of Mo films. The corrosion potential (E$_{corr}$) from the Tafel equation indicates the reaction rate of oxidation on the metal surface. A large E$_{corr}$ value corresponds to a strong oxidizing agent because the metal oxide was rapidly formed. On
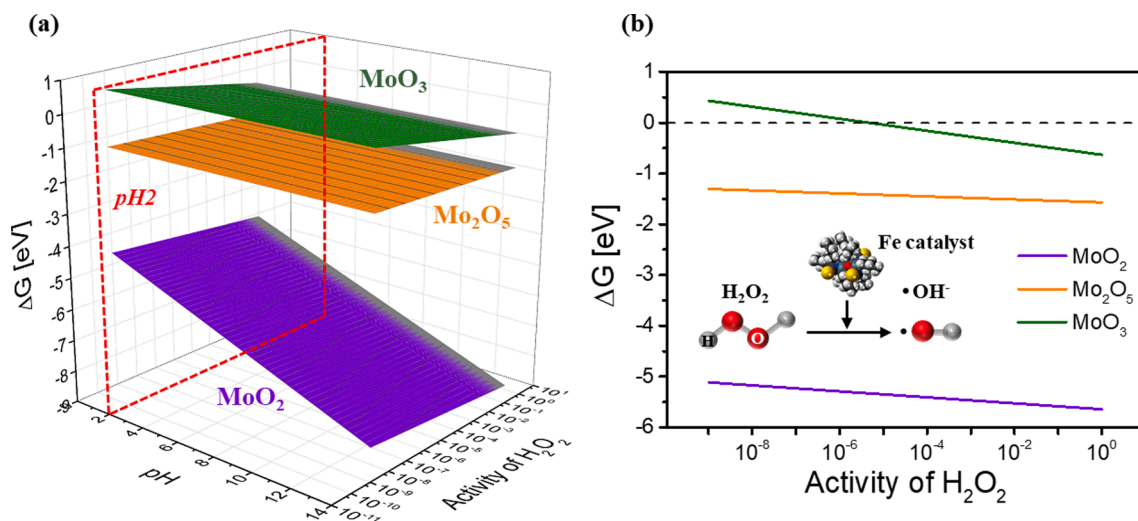
Fig. 4. Free energy of Mo oxide formation reactions as a function of activity of H_2O_2 (α_{H2O2}) (a) across pH values and (b) at pH 2.
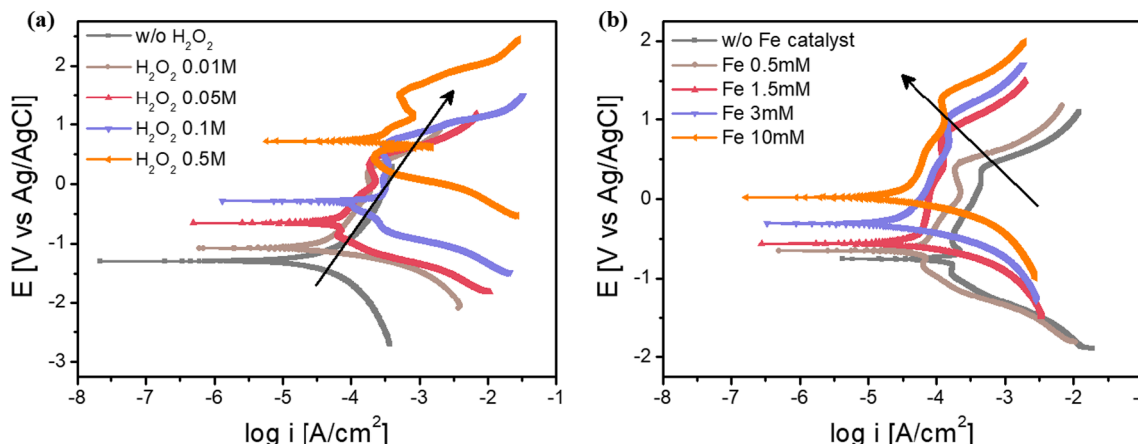

Fig. 5. Potentiodynamic polarization curves of Mo films as a function of different oxidizers: (a) H_2O_2 and (b) $Fe(NO_3)_3$.

the other hand, corrosion current density (I_{corr}) represents the amount of dissolution following the oxidation reaction. Therefore, increase in the I_{corr} value indicates active dissolution of metal film. Fig. 5(a) represents the potentiodynamic polarization curves of Mo films as a function of H_2O_2 oxidizer. Under conditions without H_2O_2, E_{corr} and I_{corr} were -1.28 V and 0.12 A/cm^2, respectively, as the smallest values. However, as the concentration of H_2O_2 increased from 0.01 M to 0.5 M, the Tafel curve shifted to the right, and both potential and current values were increased. This result is due to increases in the rate and amount of Mo oxide formation, resulting in an increased E_{corr} value. Additionally, the I_{corr} value was dramatically increased in 0.5 M of H_2O_2 because the proportion of the soluble MoO_3 phase increased. The observation is consistent with the DFT calculation results, where the surface O-vacancies are thermodynamically favorable to form only on MoO_3, but not on MoO_2 nor Mo_2O_5 surfaces as shown in Figure S5. The prevalence of oxygen vacancies on the surface of Mo and the non-localized charge distribution around the vacancy encourage interactions with high hydroxyl concentrations in H_2O_2 solution, thus promoting the dissolution of bulk MoO_3. In contrast, Fig. 5(b) shows the potentiodynamic polarization curves of Mo films as a function of Fe catalyst. In the experiments with Fe catalyst, we observed the same tendency as the H_2O_2 oxidizer showing that the rate of oxidation increases according to the Fe concentration, and thus the E_{corr} value gradually increases. However, since Fe catalyst acts as a relatively weak oxidizer compared to H_2O_2, the increase in E_{corr} value is half that of H_2O_2 oxidizer. The most important

finding in the experimental results shown in Fig. 5(b) is that, although the E_{corr} value slightly increased, the I_{corr} value decreased. This is due to the fact that although the Mo oxide formation reaction proceeded, the dissolution reaction was nearly absent because mainly insoluble MoO_2 and Mo_2O_5 phases were formed. Therefore, we confirmed that the behaviors of E_{corr} and I_{corr} derived through potentiodynamic polarization experiment agree with the previous XPS and calculated reaction free energy results. The detailed values are shown in Table 2.

3.4. CMP evaluation and surface characteristics

Fig. 6 presents the removal and dissolution rates of Mo films according to different concentrations of H_2O_2 and Fe catalyst under different experimental conditions and Mo surface roughness analyzed through AFM measurements. As shown in Fig. 6(a), the removal rate of the Mo film gradually increased as the concentration of H_2O_2 increased, due to the large amounts of Mo metal chemically reacted with H_2O_2 and converted to the Mo oxide phase. As a result, the formation of weak interfaces between Mo metal and Mo oxide became more active, suggesting a strong effect of mechanical abrasion during the CMP process. However, since a large amount of soluble MoO_3 phase was formed under excessive H_2O_2 conditions, the dissolution of Mo increased and the static etch rate (SER) of Mo film also increased sharply. Fig. 6(b) represents the surface roughness of Mo films. Each R_q and R_{pv} value means root-mean-square roughness and peak-to-valley roughness of Mo films,

Table 2

E_{corr} (corrosion potential) and I_{corr} (corrosion current density) values of Mo films for each concentration containing H_2O_2 and $Fe(NO_3)_3$.

	In H_2O_2 circumstances					In $Fe(NO_3)_3$ circumstances				
	w/o	0.01 M	0.05 M	0.1 M	0.5 M	w/o	0.5 mM	1.5 mM	3 mM	10 mM
E_{corr} [V]	−1.28	−1.07	−0.67	−0.28	0.75	−0.78	−0.67	−0.53	−0.29	0.03
I_{corr} [mA/cm^2]	0.12	0.14	0.25	0.29	0.85	0.32	0.25	0.17	0.16	0.14
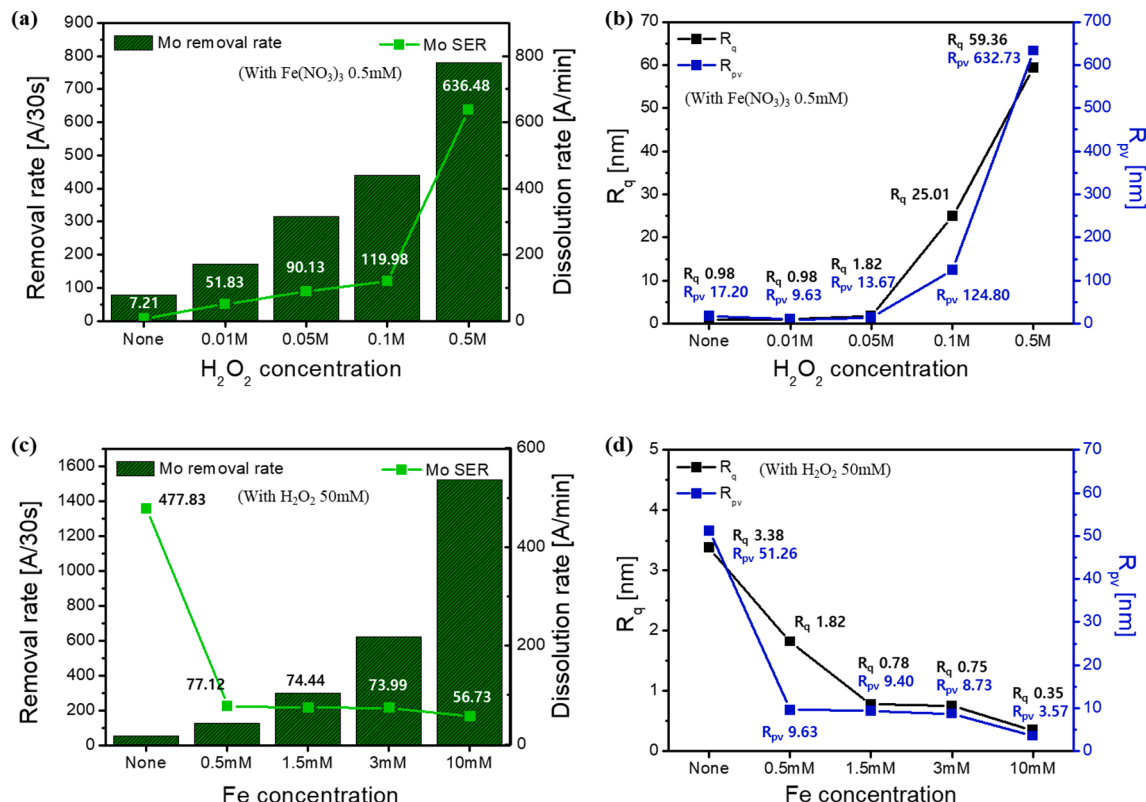
Fig. 6. (a) CMP and SER performances, (b) surface roughness of Mo films as a function of H_2O_2 concentration. (c) CMP and SER performances, (d) surface roughness of Mo films as a function of Fe concentration.

respectively. As the soluble phase of Mo oxide is generated, when the dissolution amount of Mo ions is enhancing (i.e. in case of large SER), the roughness of the top Mo surface deteriorates leading to the increase in the both R_q and R_{pv} values. Therefore, it can be seen that the accelerating trend of SER value coincides with the change in the R_q and R_{pv} values.

In contrast, when the concentration of Fe catalyst was increased under the condition of constant 50 mM H_2O_2, a high removal rate of Mo film was achieved and the dissolution rate was simultaneously minimized as shown in Fig. 6(c), especially for 10 mM of $Fe(NO_3)_3$. This is due to the sufficient in-situ oxidation, while the insoluble Mo oxide phases (i.e., MoO_2 and Mo_2O_5) were predominantly maintained. The adoption of Fe catalyst resulted in the lowest SER of 56.7 Å/min, despite the high Mo removal rate of 1500 Å per 30 s. In the experiment using the Fe catalyst, Fig. 6(d) confirms that the roughness of Mo surface was improved according to the Fe concentration, while the R_q, R_{pv} and SER values showed same tendency. These results agree well with the Mo oxidation behavior and surface analysis observed using XPS, potentiostat, and free-energy calculation results as described above. Detailed AFM images for each experimental condition are shown in Figure S6.

Table S1 shows the inductively coupled plasma mass spectrometer (ICP-MS) results for quantitative calculation of Mo dissolution. After the SER experiment, the amount of Mo ions remaining in the slurry was measured. The residual amount of Mo ions was consistent with the Mo dissolution rate as evaluated by SER test. Low dissolution of 0.882 ppm

was confirmed under the conditions of 0.05 M of H_2O_2 with 10 mM of Fe catalyst, which resulted in the highest Mo removal rate and low SER. It is noted that the detected Mo ion amount is not significantly changed as Fe catalyst increasing from 1.5 mM to 10 mM under the constant H_2O_2 concentration even though there was remarkable change when Fe was absent or 1.5 mM added. This result was interpreted as the fact that the concentration of H_2O_2 was as small as 0.05 M. Since the amount of H_2O_2 reactant is limited as 0.05 M, the change in the Mo ion concentration was not noticeable even when the Fe concentration increased, which is consistent with the SER results in Fig. 6(b).

4. Conclusions

We demonstrated that the oxidation state of Mo can be controlled through catalytic-oxidation reactions by simultaneously applying an H_2O_2 oxidizer and Fe catalyst. The use of Fe catalyst with trace amounts of H_2O_2 accelerated the H_2O_2 decomposition reaction and resulted in high hydroxyl radical generation efficiency. The synergistic reaction between oxidizer and catalyst chiefly forms insoluble MoO_2 and Mo_2O_5 phases while minimizing the generation of the soluble MoO_3 phase by modulating the Mo oxidation state, compared to the simple oxidation reaction using H_2O_2. In addition, we investigated the thermodynamic rationale by confirming the free energies of various Mo oxide phases that can be made under different oxidizer and Fe catalyst conditions by DFT calculations and analyses of dissolution kinetics. The electrochemical

oxidation and dissolution behaviors of various Mo oxide phases after the catalytic-oxidation were consistent with surface analysis and theoretical considerations. Finally, when applied to the CMP process, simultaneously applying an H_2O_2 oxidizer and Fe catalyst resulted in an improved Mo removal rate of 1500 Å per 30 s and validated a low dissolution rate of 56.7 Å/min compared to trials using single H_2O_2 as an oxidizer. We anticipate these results supported by experimental and theoretical considerations will be helpful to reduce crucial defects in next-generation semiconductor processes as well as guaranteeing neat Mo surface with less corrosion.

CRediT authorship contribution statement

Kangchun Lee: Conceptualization, Visualization, Writing - original draft. **Seho Sun:** Designed the experiments. **Hyunseok Ko:** Verified the simulated calculations. **Sung Beom Cho:** Verified the simulated calculations. **Ganggyu Lee:** Performed the experiments. **Dongsoo Lee:** Performed the experiments. **Taeseup Song:** Supervision, Writing - review. **Ungyu Paik:** Supervision, Writing - review.

Declaration of Competing Interest

The authors declare that they have no known competing financial interests or personal relationships that could have appeared to influence the work reported in this paper.

Data availability

No data was used for the research described in the article.

Acknowledgment

Appendix A. Supplementary data

Supplementary data to this article can be found online at https://doi.org/10.1016/j.apsusc.2023.156330.

References

[1] A. Micallef, C. Stiewe, G. Oppitz, E. MuLler,, High-Temperature Specific Contact Resistance Of Iron Disilicide Soldered To Molybdenum By Field's Metal, Acs Applied Electronic Materials 3 (2021) 890–897.

[2] G. Yang, P. He, X.-P. Qu, Inhibition Effect Of Glycine On Molybdenum Corrosion During Cmp In Alkaline H2o2 Based Abrasive Free Slurry, Appl. Surf. Sci. 427 (2018) 148–155.

[3] X. Wang, P. He, G. Yang, X.-P. Qu, Effect Of Coxmoy As Single Barrier Layer On Properties Of Directly Electroplated Copper Films, J. Electrochem. Soc. 163 (2016) D794.

[4] X. Wang, L.-A. Cao, G. Yang, X.-P. Qu, Study Of Direct Cu Electrodeposition On Ultra-Thin Mo For Copper Interconnect, Microelectron. Eng. 164 (2016) 7–13.

[5] F. Kaufman, D. Thompson, R. Broadie, M. Jaso, W. Guthrie, D. Pearson, M. Small, Chemical-Mechanical Polishing For Fabricating Patterned W Metal Features As Chip Interconnects, J. Electrochem. Soc. 138 (1991) 3460.

[6] M.K. Poddar, P. Jalalzai, S. Sahir, N.P. Yerriboina, T.-G. Kim, J.-G. Park, Tungsten Passivation Layer (Wo3) Formation Mechanisms During Chemical Mechanical Planarization In The Presence Of Oxidizers, Appl. Surf. Sci. 537 (2021), 147862.

[7] R. Manivannan, S. Ramanathan, The Effect Of Hydrogen Peroxide On Polishing Removal Rate In Cmp With Various Abrasives, Appl. Surf. Sci. 255 (2009) 3764–3768.

[8] X.-P. Qu, G. Yang, P. He, H. Feng, Chemical Mechanical Polishing Of Mo Using H2o2 As Oxidizer In Colloidal Silica Based Slurries, Ecs Journal Of Solid State Science And Technology 6 (2017) P470.

[9] H.-Y. Ryu, L. Teugels, K. Devriendt, H. Struyf, T.-G. Kim, J.-G. Park, Effects Of H2o2 And Ph On The Chemical Mechanical Planarization Of Molybdenum, Ecs Journal Of Solid State Science And Technology 10 (2021), 094001.

[10] J. Seo, J.H. Kim, M. Lee, K. You, J. Moon, D.-H. Lee, U. Paik, Multi-Objective Optimization Of Tungsten Cmp Slurry For Advanced Semiconductor Manufacturing Using A Response Surface Methodology, Mater. Des. 117 (2017) 131–138.

[11] K. Lee, S. Sun, G. Lee, G. Yoon, D. Kim, J. Hwang, H. Jeong, T. Song, U. Paik, Galvanic Corrosion Inhibition From Aspect Of Bonding Orbital Theory In Cu/Ru Barrier Cmp, Sci. Rep. 11 (2021) 1–10.

[12] Y. Mu, M. Zhong, K.J. Rushing, Y. Li, D.A. Shipp, Benzotriazole As A Passivating Agent During Chemical Mechanical Planarization Of Ni–P Alloy Substrates, Appl. Surf. Sci. 315 (2014) 190–195.

[13] K. Lee, J. Seo, Suppression Of Dissolution Rate Via Coordination Complex In Tungsten Chemical Mechanical Planarization, Appl. Sci. 12 (2022) 1227.

[14] O.Z. Usluer, M. Abbas, G. Wantz, L. Vignau, L. Hirsch, E. Grana, C. Brochon, E. Cloutet, G. Hadziioannou, Metal Residues In Semiconducting Polymers: Impact On The Performance Of Organic Electronic Devices, ACS Macro Lett. 3 (2014) 1134–1138.

[15] J. Seo, Chemical Mechanical Planarization-Related To Contaminants: Their Sources And Characteristics, In: Emerging Contaminants, Intechopen, 2020.

[16] J. Seo, S.H. Vegi, S. Babu, Post-Cmp Cleaning Solutions For The Removal Of Organic Contaminants With Reduced Galvanic Corrosion At Copper/Cobalt Interface For Advanced Cu Interconnect Applications, Ecs Journal Of Solid State Science And Technology 8 (2019) P379.

[17] B.-J. Cho, S. Shima, S. Hamada, J.-G. Park, Investigation Of Cu-Bta Complex Formation During Cu Chemical Mechanical Planarization Process, Appl. Surf. Sci. 384 (2016) 505–510.

[18] G.B. Basim, I.U. Vakarelski, B.M. Moudgil, Role Of Interaction Forces In Controlling The Stability And Polishing Performance Of Cmp Slurries, Journal Of Colloid And Interface Science 263 (2003) 506–515.

[19] K. Lee, J. Seo, U. Paik, Preparation And Characterization Of Slurry For Cmp, in: Advances In Chemical Mechanical Planarization (Cmp), Elsevier, 2022, pp. 323–354.

[20] Y. Yang, Q. Wang, R. Aleisa, T. Zhao, S. Ma, G. Zhang, T. Yao, Y. Yin, Mos2/Fes Nanocomposite Catalyst For Efficient Fenton Reaction, ACS Appl. Mater. Interfaces (2021).

[21] D.C. Luehrs, A.E. Roher, Demonstration Of The Fenton Reaction, J. Chem. Educ. 84 (2007) 1290.

[22] R. Liang, Y. Li, M. Huo, H. Lin, Y. Chen, Triggering Sequential Catalytic Fenton Reaction On 2d Mxenes For Hyperthermia-Augmented Synergistic Nanocatalytic Cancer Therapy, ACS Appl. Mater. Interfaces 11 (2019) 42917–42931.

[23] A.A. Vitale, E.A. Bernatene, M.G. Vitale, A.B. Pomilio, New Insights Of The Fenton Reaction Using Glycerol As The Experimental Model. Effect Of O2, Inhibition By Mg2+, And Oxidation State Of Fe, Chem. A Eur. J. 120 (2016) 5435–5445.

[24] K. Choudhary, K.F. Garrity, A.C. Reid, B. Decost, A.J. Biacchi, A.R.H. Walker, Z. Trautt, J. Hattrick-Simpers, A.G. Kusne, A. Centrone, The Joint Automated Repository For Various Integrated Simulations (Jarvis) For Data-Driven Materials Design, npj Comput. Mater. 6 (2020) 1–13.

[25] M. Chase, C. Davies, J. Downey, D. Frurip, R. Mcdonald, A. Syverud, Nist-Janaf Thermochemical Tables. Nist Stand. Ref, Database (1985).

[26] A.K. Singh, L. Zhou, A. Shinde, S.K. Suram, J.H. Montoya, D. Winston, J. M. Gregoire, K.A. Persson, Electrochemical Stability Of Metastable Materials, Chem. Mater. 29 (2017) 10159–10167.

[27] G. Kresse, J. Furthmüller, Efficiency Of Ab-Initio Total Energy Calculations For Metals And Semiconductors Using A Plane-Wave Basis Set, Comput. Mater. Sci 6 (1996) 15–50.

[28] G. Kresse, D. Joubert, From Ultrasoft Pseudopotentials To The Projector Augmented-Wave Method, Phys. Rev. B 59 (1999) 1758.

[29] J.J. Mortensen, L.B. Hansen, K.W. Jacobsen, Real-Space Grid Implementation Of The Projector Augmented Wave Method, Phys. Rev. B 71 (2005), 035109.

[30] T.K. Woo, P.M. Margl, P.E. Blöchl, T. Ziegler, A Combined Car– Parrinello Qm/Mm Implementation For Ab Initio Molecular Dynamics Simulations Of Extended Systems: Application To Transition Metal Catalysis, J. Phys. Chem. B 101 (1997) 7877–7880.

[31] P.E. Blöchl, O. Jepsen, O.K. Andersen, Improved Tetrahedron Method For Brillouin-Zone Integrations, Phys. Rev. B 49 (1994) 16223.

[32] J. Perdew, K. Burke, M. Ernzerhof, Perdew, Burke, And Ernzerhof Reply, Phys. Rev. Lett. 80 (1998) 891.

[33] J. Neugebauer, M. Scheffler, Adsorbate-Substrate And Adsorbate-Adsorbate Interactions Of Na And K Adlayers On Al (111), Phys. Rev. B 46 (1992) 16067.

[34] M. Ürgen, U. Stolz, R. Kirchheim, Esca Measurements Of Films On Molybdenum Formed In The Passive And Transpassive Region, Corros. Sci. 30 (1990) 377–391.

[35] D.O. Scanlon, G.W. Watson, D. Payne, G. Atkinson, R. Egdell, D. Law, Theoretical And Experimental Study Of The Electronic Structures Of Moo3 And Moo2, J. Phys. Chem. C 114 (2010) 4636–4645.

[36] J. Baltrusaitis, B. Mendoza-Sanchez, V. Fernandez, R. Veenstra, N. Dukstiene, A. Roberts, N. Fairley, Generalized Molybdenum Oxide Surface Chemical State Xps Determination Via Informed Amorphous Sample Model, Appl. Surf. Sci. 326 (2015) 151–161.

[37] S. Tamilmani, W. Huang, S. Raghavan, R. Small, Potential-Ph Diagrams Of Interest To Chemical Mechanical Planarization Of Copper, J. Electrochem. Soc. 149 (2002) G638.

[38] S.-F. Ho, S. Contarini, J. Rabalais, Ion-Beam-Induced Chemical Changes In The Oxyanions (Moyn-) And Oxides (Mox) Where M= Chromium, Molybdenum,

Tungsten, Vanadium, Niobium And Tantalum, Journal Of Physical Chemistry 91 (1987) 4779–4788.

[39] T.A. Patterson, J.C. Carver, D.E. Leyden, D.M. Hercules, A Surface Study Of Cobalt-Molybdena-Alumina Catalysts Using X-Ray Photoelectron Spectroscopy, J. Phys. Chem. 80 (1976) 1700–1708.

[40] D. Briggs, G. Beamson, Primary And Secondary Oxygen-Induced C1s Binding Energy Shifts In X-Ray Photoelectron Spectroscopy Of Polymers, Anal. Chem. 64 (1992) 1729–1736.

[41] G. Beamson, D. Briggs, High Resolution Monochromated X-Ray Photoelectron Spectroscopy Of Organic Polymers: A Comparison Between Solid State Data For Organic Polymers And Gas Phase Data For Small Molecules, Mol. Phys. 76 (1992) 919–936.

[42] Y. Wu, Y. Lin, J. Xu, Synthesis Of Ag–Ho, Ag–Sm, Ag–Zn, Ag–Cu, Ag–Cs, Ag–Zr, Ag–Er, Ag–Y And Ag–Co Metal Organic Nanoparticles For Uv-Vis-Nir Wide-Range Bio-Tissue Imaging, Photochem. Photobiol. Sci. 18 (2019) 1081–1091.

[43] J. Muff, L.R. Bennedsen, E.G. Søgaard, Study Of Electrochemical Bleaching Of P-Nitrosodimethylaniline And Its Role As Hydroxyl Radical Probe Compound, J. Appl. Electrochem. 41 (2011) 599–607.

[44] K. Kim, K. Lee, S. So, S. Cho, M. Lee, K. You, J. Moon, T. Song, Fenton-Like Reaction Between Copper Ions And Hydrogen Peroxide For High Removal Rate Of Tungsten In Chemical Mechanical Planarization, Ecs Journal Of Solid State Science And Technology 7 (2018) P91.